1-1-2008

A Dynamic Lagrangian, Field-scale Model Of Dust Dispersion From Agriculture Tilling Operations

Thomas H. Meyer
University of Connecticut, thomas.meyer@uconn.edu

A Dynamic Lagrangian, Field-Scale Model of Dust Dispersion from Agriculture Tilling Operations

J. Wang, A. L. Hiscox, D. R. Miller, T. H. Meyer, T. W. Sammis

Abstract. *Dust exposure in and near farm fields is of increasing concern for human health and may soon be facing new emissions regulations. Dust plumes of this nature have rarely been documented due to the unpredictable nature of the dust plumes and the difficulties of accurately sampling the plumes. This article presents a dynamic random-walk model that simulates the field-scale PM_{10} (particle diameter $\leq$10 μm) dust dispersion from an agriculture disking operation. The major improvements over traditional plume models are that it can simulate moving sources and plume meander. The major inputs are the friction velocity (u*), wind direction in the simulation period, atmospheric stability, and source strength (μg s^{-1}). In each time step of the model simulation, three instantaneous wind velocities (x, y, and z directions) are produced based on friction velocity, mean wind speed, and atmospheric stability. The computational time step is 0.025 times the Lagrangian time scale. The resulting instantaneous wind vectors transport all the individual particles. The particle deposition algorithm calculates if a particle is deposited based on the particle settling speed and vertical wind velocity when it touches the ground surface. The particle mass based concentration in 3-D can be obtained at any instant by counting the particle numbers in a unit volume and then converting to mass based on the particle size and density. Simulations from this model are verified by comparison with dust dispersion and plume concentrations obtained by an elastic backscatter LIDAR. The simulated plume spread parameters (σ_y, σ_z) at downplume distances up to 160 m were within ±73% of those measured with a remote aerosol LIDAR. Cross-correlations between a modeled plume and LIDAR measurements of the actual plume were as high as 0.78 near the ground and decreased to 0.65 at 9 m above ground, indicating close pattern similarity between the modeled and measured plumes at lower heights but decreasing with elevation above the ground.*

Keywords. *Disking, Dust, Field scale, Lagrangian transport, Laser radar, LIDAR, Near-field, Particulate matter, PM_{10}, Random walk model.*

Particulate matter (PM) of aerodynamic diameter less than or equal to 10 microns, PM_{10}, is regulated by the U.S. Environmental Protection Agency (EPA) as part of the National Ambient Air Quality Standard (NAAQS) pollutants. PM_{10} is directly emitted from a wide range of industrial point sources (e.g., power plants, incinerators, cement plants), mobile sources (e.g., automobiles and trucks), and nonpoint sources such as agricultural operations (e.g., field operations, harvesting, cattle ranches) and construction sites. PM_{10} emitted from agriculture field operations (e.g., disking, listing, leveling, planting, harvesting) is first dispersed downwind in the near-field in high-concentration plumes and is then dispersed in lower concentrations further downwind in the far-field (i.e., >1 km) (Hanna et al., 1982). Plume movement from the source to the boundary between near-field and far-field is dynamic and depends on the temporal and spatial dynamics of the wind, turbulence, and stability conditions. PM_{10} exposure to farmers in their fields and people nearby is generally expected to be high-density, short-event doses (Hiscox et al., 2008).

The theoretical ensemble average represented by Gaussian dispersion is made up of individual events that are widely distributed in their initial path directions and speeds and are changing on time scales of seconds to minutes. Only limited attempts to model individual near-field dispersion events have been made, and the majority of these have been in urban areas (Coirier and Kim, 2006a, 2006b; Flaherty et al., 2007; Hamel et al., 2006; Haupt et al., 2007). Several near-source unpaved road dust modeling studies have been conducted with steady-state Gaussian models, such as the EPA ISCST3, or Industrial Source Complex Short Term model (EPA, 1995), by considering the road dust as a constant line source (Verdanth et al., 2004; Etyemezian et al., 2004; Etyemezian et al., 2003; Chow et al., 1999). Drawbacks to using Gaussian models for modeling near-field dust dispersion from agriculture operations are the model requirements of steady-state environmental conditions and releases from a continuous fixed-location line or point source. Agriculture sources of PM_{10} are most often moving sources because the operation equipment is traveling continuously in the field.

Eulerian dynamic models, based on the atmospheric diffusion equation, have also been developed to simulate unpaved road dust dispersion (e.g., Veranth et al., 2004; Etyemezian

Submitted for review in April 2008 as manuscript number SE 7456; approved for publication by the Structures & Environment Division of ASABE in August 2008.

The authors are **Junming Wang, ASABE Member,** Research Scientist, Department of Plant and Environmental Sciences, New Mexico State University, Las Cruces, New Mexico; **April L. Hiscox, ASABE Member,** Assistant Professor, **David R. Miller, ASABE Member,** Professor, and **Thomas H. Meyer,** Associate Professor, Department of Natural Resources Management and Engineering, University of Connecticut, Storrs, Connecticut; and **Ted W. Sammis, ASABE Member,** Professor, Department of Plant and Environmental Sciences, New Mexico State University, Las Cruces, New Mexico. **Corresponding author:** Junming Wang, Department of Plant and Environmental Sciences, New Mexico State University, MSC3Q, Box 30003, Las Cruces, NM 88003; phone: 575-646-3239; fax: 575-646-6041; e-mail: jwang@nmsu.edu.

  ISSN 0001–2351

et al., 2003). However, applying Eulerian models for estimating scalar transfer by turbulence has been limited by their inability to accurately model the dispersion of material from near-field sources (Van den Hurk and Baldocchi, 1990).

Lagrangian models do not suffer from this deficiency because they explicitly consider the diffusion of material in both the near-field and the far-field (Van den Hurk and Baldocchi, 1990). Lagrangian models that simulate gas and particle trajectories in three dimensions from steady-state continuous, fixed point, line, and area sources have been reported (e.g., Aylor and Flesch, 2001; Aylor and Ferrandino, 1989; Wilson and Shum, 1992). In these models, particle movements are driven by wind velocities calculated in each time step (Δt) from inputs of mean wind speed, direction, and turbulence statistics. The final particle or puff number concentration at a point is calculated as the particle number divided by the local volume. Wang et al (1995) utilized a Lagrangian model to describe the movement of spray aerosols released from a moving aircraft. The model prediction was adequate in two-dimensional steady wind conditions, but was less accurate in variable wind conditions. However, to our knowledge, no Lagrangian model has been reported to predict the dynamics and concentrations of individual near-field events during agriculture tilling operations. We have developed a dynamic field-scale (near-field) model for dust dispersion simulations from an agriculture operation (disking). The objective of this article is to present the model and its initial validation.

Simulation Model

A Lagrangian simulation model was developed to simulate the dynamic, three-dimensional PM_{10} near-field dust dispersion and concentrations (μg m^{-3}) from agricultural field preparation operations (fig. 1). The model physics follow the theory and methods of Aylor and Ferrandino (1989), Wilson and Shum (1992), Wang et al. (1995), and Aylor and Flesch (2001). The model described here adapts the previous theory to moving sources and is driven by dynamic, rather than steady-state, meteorological inputs. This model was programmed in the C^{++} computer language as a user-friendly software package and excludes any particles generated by the farming equipment that are larger than 10 μm b ecause most (96%) of the total dust mass in the air is PM_{10} (Holmén et al., 2008).

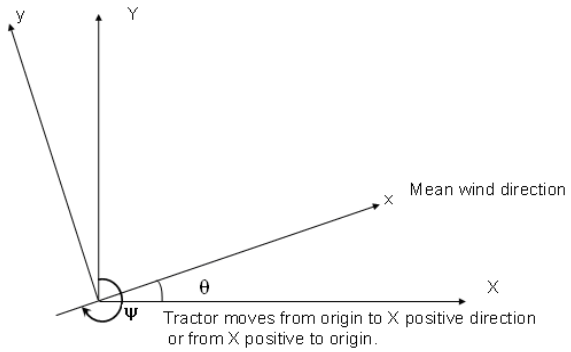

Figure 1. Simulation coordinate systems.

The model consists of three major components (submodels): the turbulent wind field and Lagrangian time scale, particle flight, and particle deposition. The overall structure of the model is depicted in figure 2. By taking source strength, atmospheric data, and simulation time period length as inputs, the model predicts the dynamic three-dimensional PM_{10} concentrations. The PM particle flights are driven by the turbulent wind field, and each simulation time step length is determined by the Lagrangian time scale. During each particle flight in each time step, the deposition algorithm judges if the particle will be deposited on the ground. The model first simulates the 2000 nm particle flight, deposition, and concentration. Then, the concentrations of other PM_{10} size classes are estimated from the 2000 nm simulation. Finally, the concentrations are scaled by the source strength, and their sums are outputted as the PM_{10} concentration. The detailed theoretical considerations of the model are described as in the following paragraphs.

Inputs and Outputs

The model inputs include simulation time period length t(s), PM_{10} source strength Q (μg s^{-1}), friction velocity u^* (m s^{-1}), mean wind direction ψ (°), and Monin-Obukhov length L (m) for each 1 s period of the simulation. The model outputs are the 3-D concentration values $c(X, Y, Z, t)$ (μg m^{-3}) in both space and time. The symbols and definitions are listed in the Appendix.

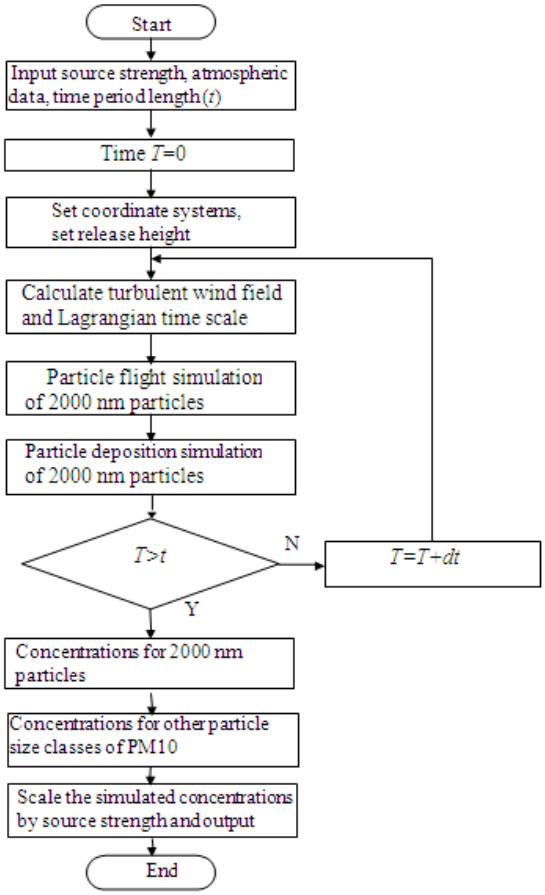

Figure 2. Flowchart of the overall model.

Model Formulations

Simulation Coordinate Systems

Two Cartesian coordinate systems were adopted (fig. 2). One was a fixed right-hand coordinate system (*X*, *Y*, *Z*) that defines the coordinates for the inputs and outputs. The positive *X* axis points in the direction that the tractor moves, and positive *Z* is the height above ground (ground level = 0). The second coordinate system (*x*, *y*, *z*) is also a right-hand system, but it is adaptive through the modeling process. The positive *x* axis points in the direction that the wind is blowing toward for each simulation period. Following the normal meteorological convention, the wind direction (ψ, °) is the direction that the wind is blowing from. The parameter ψ is one input of the model. The two coordinate systems share the same *Z* axis. The angle between the *x* and *X* axes is θ (°), which shows the mean wind direction. The coordinate conversion from the *x*, *y*, *z* system to the *X*, *Y*, *Z* system is:

$$\begin{aligned} X &= \cos(\theta) - y\sin(\theta) \\ Y &= \sin(\theta) + y\cos(\theta) \\ Z &= z \end{aligned} \tag{1}$$

Particle Flight

Turbulent airflow along a particle trajectory is simulated by a three-dimensional Lagrangian stochastic model. The model follows Wang et al. (1995) and satisfies the well-mixed criterion (Thompson, 1987). "Simply stated, the well-mixed criteria requires that an initially well-mixed cloud of particles in an infinite domain should remain well-mixed. The importance of the criteria is that it states the constraint implied by the Eulerian probability density functions upon possible Lagrangian stochastic models" (Flesch and Wilson, 1992). Since PM_{10} particles are small (<300 μm), the inertia "crossing trajectory" effect is ignored (Csanady, 1963; Sawford and Guest, 1991) and the particles are treated as passive scalars, i.e., the particles are only moved by the wind and no particle inertia is considered.

The random flight of each dust particle is simulated as a Markov process in a sequence of short time steps after Wilson and Shum (1992), during each of which the particle moves by:

$$dx = (\bar{u}(z) + u)dt,\ dy = vdt,\ dz = (w - v_s)dt \tag{2}$$

where $\bar{u}(z)$ is the mean wind velocity for the modeling period (m s^{-1}); *u*, *v*, and *w* are the instantaneous along-wind, cross-wind, and vertical turbulent velocities, respectively (m s^{-1}); v_s is the settling velocity of the particle (m s^{-1}); and *dt* is the time duration of a time step (s).

The velocity fluctuations are formulated as (Wilson and Shum, 1992):

$$u = q_u\sigma_u,\ v = q_v\sigma_v,\ w = q_w\sigma_w \tag{3}$$

where σ_u, σ_v, and σ_w are the standard deviations of *u*, *v*, and *w*; the *q* values are dimensionless parameters from:

$$q_u^{t+dt} = \alpha q_u^{(t)} + \beta[c_u r_u^{t+dt} + c_w r_w^{t+dt}] \tag{4}$$

$$q_v^{t+dt} = \alpha q_v^{(t)} + \beta r_v^{t+dt} \tag{5}$$

$$q_w^{t+dt} = \alpha q_w^{(t)} + \beta r_w^{t+dt} + \gamma\tau_L \frac{\partial\sigma_w}{\partial z} \tag{6}$$

where τ_L (s) is the passive fluid Lagrangian time scale, defined in the next section, and $dt = 0.025\tau_L$ (s) after Aylor and Flesch (2001).

The α, β, and γ parameters in equations 4 through 6 are defined by Wilson and Shum (1992) as follows:

$$\alpha = 1 - \frac{dt}{\tau_L} \tag{7}$$

$$\beta = \sqrt{1 - \alpha^2} \tag{8}$$

$$\gamma = 1 - \alpha \tag{9}$$

The *r* values, dimensionless random Gaussian variables, in equations 4 through 6 are mutually independent, each having zero mean and unit variance. Parameters c_u and c_w in equation 4 are defined from (Wilson and Shum, 1992):

$$c_w = -\frac{u^{*2}}{\sigma_u\sigma_w} \tag{10}$$

$$c_u = \sqrt{1 - c_w^2} \tag{11}$$

Turbulent Wind Field and Lagrangian Time Scale

The mean wind speed variation with height above ground is described by the traditional, stability-adjusted logarithmic profile, $\bar{u}(z)$, and calculated by:

$$\bar{u}(z) = \frac{u^*}{k}\left[\ln\left(\frac{z}{z_0}\right) + \varphi\left(\frac{z}{L}\right)\right] \tag{12}$$

where *k* is the von Karman constant (0.4; Stull, 2001), and z_0 is the roughness length of the operating field (0.002 m; Campbell and Norman, 1998; Stull, 2001).

The Lagrangian time scale of the passive fluid, τ_L, is a function of stability and inversely related to the vertical velocity perturbations given by Wilson and Shum (1992):

$$\tau_L = \frac{l}{\sigma_w} \tag{13}$$

where the length scale *l* is given by:

$$l = 0.5z\left(1 + 5\frac{z}{L}\right)^{-1} \text{ for } L \geq 0 \tag{14}$$

$$l = 0.5z\left(1 - 6\frac{z}{L}\right)^{1/4} \text{ for } L < 0 \tag{15}$$

During stable conditions, the standard deviations of velocity (σ_u, σ_v, and σ_w, m s^{-1}) are assumed constant in the surface layer, and:

$$\sigma_u = \sigma_v = 2.4u^* \text{ for } L \geq 0 \tag{16}$$

$$\sigma_w = 1.25u^* \text{ for } L \geq 0 \tag{17}$$

For convective conditions, the formulations of Panofsky et al. (1977) and Panofsky and Dutton (1984) are used:

$$\sigma_u = \sigma_v = u^* \left[4 + 0.6 \left(\frac{z_i}{-L} \right)^{2/3} \right]^{1/2} \quad \text{for } L < 0 \qquad (18)$$

$$\sigma_w = 1.25 u^* \left[1 - 3 \cdot \frac{z}{L} \right]^{1/3} \quad \text{for } L < 0 \qquad (19)$$

where the mixing layer height, z_i, is estimated as 1000 m unless measurements are available.

Particle Deposition

The particle deposition algorithm follows Aylor and Ferrandino (1989). If the height z of a particle at the beginning of a time step is within the range $0 < z < (-w + v_s) \cdot dt$, then the particle will reach the ground during the time step. The fraction of these actually deposited (P_G) is:

$$P_G(w) = 2 \cdot v_s / (v_s - w), \; w \le -v_s \qquad (20)$$

$$P_G(w) = 1, \; |w| < v_s \qquad (21)$$

A random number R_n is chosen from a uniform distribution between 0 and 1 for each line-of-flight segment. If R_n is less than P_G, then the particle is deposited on the ground. If the particle is not deposited, it is reflected. The new height of the particle is:

$$z = |z_{t-1} - 2 v_s dt| \qquad (22)$$

where z_{t-1} is the position of the particle at the previous time step.

Release Height for the Disking Experiment

Examination of photos, such as figure 3, showed continuous dust swirls behind the tractor as it moved across the field. Since the transport solutions are quite sensitive to the height above the ground, this initial particle rise at the source is generally parameterized by raising the particle release height above the ground level. For example, Etyemezian et al. (2004) set their initial plume height center line at 1.5 m for a Gaussian model of unpaved road dust from a passing vehicle (EPA IST3 model). We estimated the particle release height (H) from the product of the implement-induced upwardly displaced air velocity (V_d) and the maximum time for a particle to disperse to the downwind edge of the implement (t_{max}). V_d is taken as equal to the tractor speed (average speed = 1.4 m s^{-1}), and t_{max} (1.1 s) is the quotient of the implement width (4 m) divided by the mean wind speed (3.7 m s^{-1}):

$$H = V_d t_{\max} = (1.4)(1.1) = 1.5m \qquad (23)$$

Simulation Implementation for the Disking Experiment

The tractor movement on the X axis, from origin to the X positive direction or from the X positive direction to origin, is divided into segments. Each segment is 0.5 m in length and is assumed to be an instantaneous puff source. When the tractor moves into a segment, 30,000 particles are released from the particle class with geometric mean diameters 2000 nm. These values are based on measurement near the source. The PM_{10} particle size distribution, in the simulation shown herein, was measured by Holmén et al. (2008) and is presented in table 1. For the case of a disking implement, each point re-

Figure 3. Disking operation and resulting dust plume.

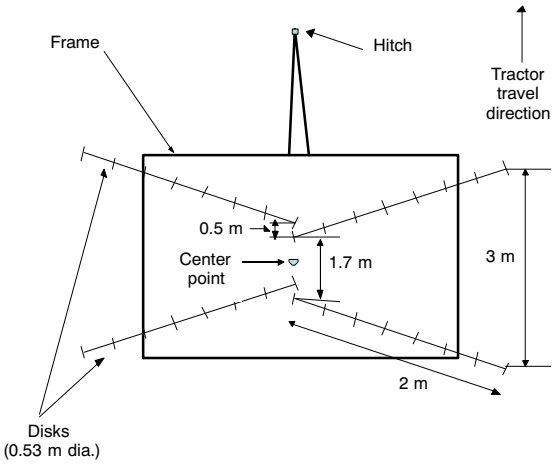

Figure 4. Spatial locations of disks (John Deere T0310, Deere and Co., Moline, Ill.).

lease is 30,000/32 based on the 32 disks on the implement, as shown in figure 4.

The wind direction, speed, and atmospheric stability are not steady over the simulation period, which in this case is the 3 min required for the tractor to traverse the field. Thus, we use short time periods, on the scale of 1.0 s, to input atmospheric data to drive the simulation. One-second averages of u^*, wind direction, and L measured by an in-field sonic anemometer are used (fig. 5).

CPU resources are generally limited; therefore, we only simulate the flights of the particle class of geometric mean diameter of 2000 nm, with a settling velocity of 0.0003 m s^{-1}, because the final output is the weight-based concentration and 2000 nm particles have the largest weight proportion in the particle classes (table 1). Particles less than or equal to 10 μm are all small enough that their settling speed is near zero and inertial effects are absent. Therefore, they all move in the turbulent atmosphere in the same manner, and it was necessary to model only one particle size class to simulate the entire PM_{10} distribution. If particles larger than PM_{10} were being modeled, it would be necessary to model the cross-streamline trajectory of the particles larger than ~300 μm (Wang et al., 1995, and others). But the measurements of

Table 1. Source PM_{10} particle size distribution during disking experiments based on data in Holmén et al. (2008). The settling speeds were calculated by Stoke's law.

D_p[a] Range (nm)	Particle GMD[b] (nm)	P_{number}[c]	Total Weight (μg)[d]	Total Weight Ratio[e]	Settling Speed (m s^{-1})
$7 \le D_p < 28.8$	14.2	2.70E+06	0.01	0.00003	1.3E-08
$28.8 \le D_p < 56.4$	40.3	9.00E+05	0.06	0.00025	1.0E-07
$56.4 \le D_p < 95.1$	73.2	3.30E+05	0.14	0.00054	3.4E-07
$95.1 \le D_p <159$	123	3.00E+05	0.58	0.00233	9.5E-07
$159 \le D_p < 266$	205.7	2.70E+05	2.46	0.00979	2.7E-06
$266 \le D_p < 387$	320.8	3.00E+04	1.04	0.00413	6.5E-06
$387 \le D_p < 621$	490.2	1.50E+04	1.85	0.00736	1.5E-05
$621 \le D_p <960$	772.1	1.20E+04	5.78	0.02301	3.8E-05
$960 \le D_p <1620$	1247.1	3.00E+04	60.90	0.24245	9.8E-05
$1620 \le D_p <2420$	2000	30000	251.20	1.00000	3.0E-04
$2420 \le D_p <6660$	4014.6	300	20.32	0.08088	1.0E-03
$6660 \le D_p <10060$	8185.3	90	51.66	0.20565	4.2E-03
Summation			396.00		

[a] D_p = particle diameter.
[b] GMD = geometric mean diameter.
[c] P_{number} = corresponding particle number in source, when there are 30,000 particles of 2000 nm GMD in a source release.
[d] Total weight = P_{number} × each particle weight; each particle weight = ρV, where V is the volume of each corresponding particle (eq. 25).
[e] Total weight ratio = total weight of particles in the D_p range / total weight of 2000 nm particles.

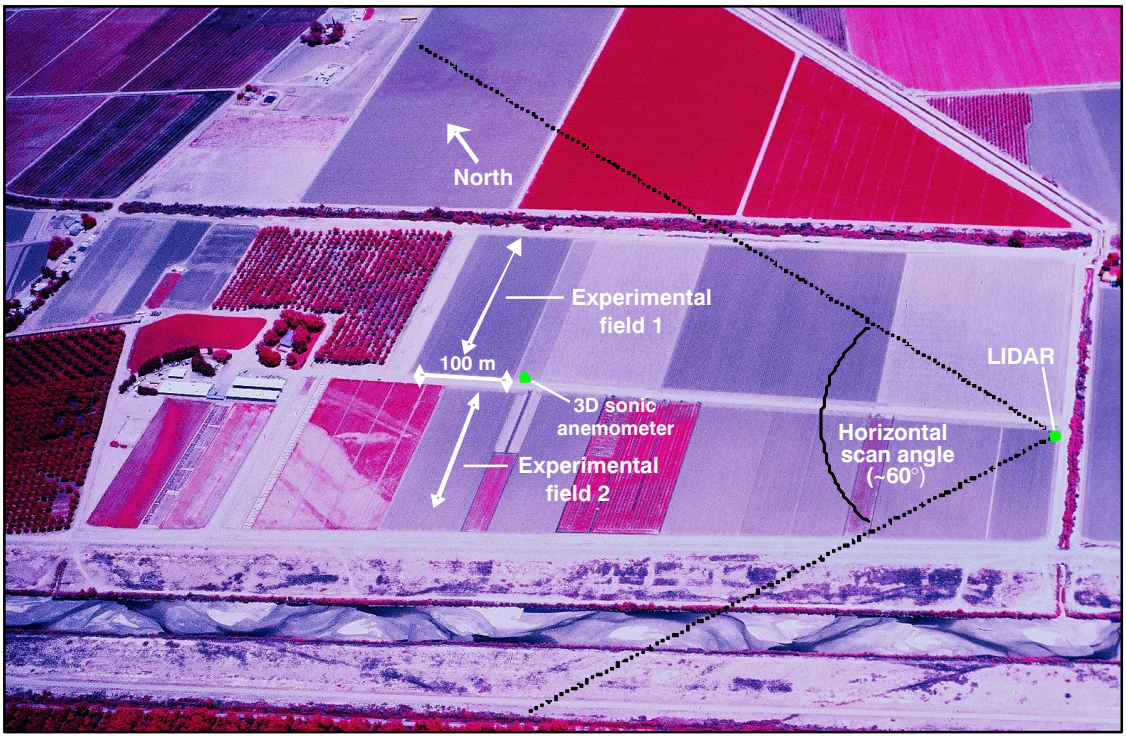

Figure 5. Experimental farm with field and sensor locations.

Holmén et al. (2008) showed that 96% of dust particles present, at the measurement height of 1.5 m, were ≤10 μm, and all of the remaining 4% were nearly as small.

Simulated Concentrations

In each simulation, the random-walk model tracks each particle until it is deposited on the ground or until the simulation time runs out. For calculating the 2000 nm particle concentration $c_{2000}(X, Y, Z, t)$ (μg m^{-3}) at a point (X, Y, Z) and at time t, a "detection cube" is defined with a side length of 1 m and volume ∇V = 1 m^3. The 2000 nm particle number ($P_{N\,2000}$) in the cube at time t is counted, and the concentration $c_{2000}(X, Y, Z, t)$ (μg m^{-3}) is:

$$c_{2000}(X,Y,Z,t) = \rho V_{2000} P_{N\,2000} / \nabla V \tag{24}$$

where ρ is the particle density, which is assumed to be 2 × 10^{-12} μg nm^{-3} (2 g cm^{-3}) for the soil type in the field study used for comparison (Wagner and Hagen, 1998), and V_{2000} is the volume of each 2000 nm particle assuming the particle is a sphere:

$$V_{2000} = \frac{4}{3}\pi r^3 \tag{25}$$

where r is the radius of the particle (2000/2 = 1000 nm).

Concentrations for Other Particle Size Classes

The concentrations in size classes other than 2000 nm are obtained by scaling their measured mass proportion by the 2000 nm simulation. For example, the concentration for the size class of geometric mean diameter 4014.6 nm at coordinate (X, Y, Z) and time t, $c_{4041.6}(X, Y, Z, t)$, is calculated by scaling equation 24:

$$c_{4041.6}(X,Y,Z,t) = \rho V_{4041.6}(P_{N\,2000} R) / \Delta V \tag{26}$$

where $V_{4041.6}$ is the volume of each 4041.6 nm particle, calculated using equation 25, and R is the particle number ratio of 2000 nm to the 4041.6 nm in each source puff (300/30000, table 1).

The procedure above is repeated for the other size classes. The total concentration $c_{total}(X, Y, Z, t)$ of all the particle classes in table 1 is the summation of concentrations in all the size classes.

Scaling the Simulated Concentrations by Source Strength

The model is run with an input Q = 350 μg s^{-1}. Actual PM_{10} concentrations $c_{PM\,10}(X, Y, Z, t)$ (μg m^{-3}) can only be obtained when the results are scaled to the true source strength. The source strength in the simulation (Q_{si}, μg s^{-1}) is the total mass of particles released in each source puff (396 μg, table 1) divided by the release time T_{re} (T_{re} = 0.5 m/V_{tr}), where V_{tr} (m s^{-1}) is the tractor speed (m s^{-1}). (The 0.5 m is the previously mentioned release segment length along the tractor path). Then:

$$Q_{si} = \frac{396}{T_{re}} \tag{27}$$

and the PM_{10} concentration $c_{PM\,10}(X, Y, Z, t)$ is:

$$c_{PM10}(X,Y,Z,t) = \frac{Q}{Q_{si}} \times c_{total}(X,Y,Z,t) \tag{28}$$

Field Verification Experiments

The model simulated the 2005 dynamic dust dispersion experiments from disking operations in an irrigated cotton field near Las Cruces, New Mexico, described by Holmén et al. (2008) and Hiscox et al. (2008). The experimental field was ~2.8 ha. Figure 5 presents an aerial photo of the site annotated with the location of the field and instrumentation. Experimental field 1 was used in the spring 2005 to measure dust emissions from the field preparation and planting operations. The field was worked six times in the spring for plowing (21 March), crushing (28 March), disking (31 March), leveling (4 April), listing (7 April), and planting (11 April) operations. The field was a mixture of Armijo clay loam and Harkey loam soil types (USDA, 2005). The soil moisture was 43% ±18%.

A 3-D sonic anemometer (CSAT3, Campbell Scientific, Inc., Logan, Utah) was located at 1.5 m height at the field edge (fig. 5) to measure the 20 Hz wind component velocities (u, v, w). The friction velocity (u*), Monin-Obukhov length (L), and wind direction were obtained for each sampling pass and each second.

Dust plume size, shape, and movement were measured remotely via the University of Connecticut portable backscatter elastic LIDAR at approximately 45 s intervals. The LIDAR specifications are listed in Hiscox et al. (2006). The LIDAR is capable of scanning in either horizontal or vertical planes. For this disking operation, a series of horizontal slices was designed to scan the entire plume (fig. 5). The lowest elevation of the scan was a horizontal slice just above the field, and successive horizontal slices were collected at increasing elevations at ~3 m intervals. A full scan consisted of 5 to 15 different elevations depending on weather conditions, and the full scans were repeated 5 or 6 times for each pass depending on the dust's persistence. A full scan (15 elevations) was completed in approximately 45 s. The slices from each scan were combined in LIDAR data analysis software to characterize the three-dimensional plume on this time scale (Hiscox et al., 2006).

LIDAR sampling was conducted during each pass and afterwards for several minutes. At the end of the pass, the tractor was stopped at the end of the field and its engine was turned off until all sampling was completed and the generated dust plume had moved out of the sampling area. Then another pass across the field was made.

The average source strength Q was 350 μg s^{-1} for 23 disking passes, determined from measurements of a GT640A sampler (Met One Instruments, Inc., Grants Pass, Ore.) and a ELPI low-pressure, cascade impactor, sampler (Dekati, Ltd., Finland) (Holmén et al., 2008; Hiscox et al., 2008).

Results and Discussion

Model Evaluation

The model performance was evaluated by comparing the modeled plume characteristics with those measured remotely with the University of Connecticut Elastic Backscatter LIDAR. Plume dispersion, plume shape, and plume concentrations and locations were compared. The average atmospheric conditions for each pass are listed in table 2.

Table 2. Average atmospheric conditions for each pass.

Pass	Time	ψ (°)	u^* (m s^{-1})	L (m)
1	11:40:40-11:43:55	17.42	0.44	-0.6
2	11:47:52-11:50:36	3.28	0.36	-0.5
3	11:57:58-12:00:52	4.52	0.46	-2.3
4	12:04:49-12:07:43	21.42	0.33	-0.7
5	13:48:51-13:51:35	353.06	0.36	-1.3
6	14:00:53-14:03:36	359.82	0.27	-0.7
7	14:13:29-14:18:35	19.51	0.39	-0.7
8	14:34:40-14:37:34	359.68	0.35	-1.4
9	14:45:23-14:48:15	349.03	0.43	-1.0
10	14:58:30-15:01:00	4.02	0.32	-0.9
11	15:13:32-15:16:20	3.39	0.32	-0.7
12	15:44:07-15:46:57	10.31	0.33	-1.3
13	15:57:10-15:59:50	20.47	0.32	-1.1
14	16:18:50-16:21:31	14.51	0.39	-1.2
15	16:46:54-16:49:45	7.42	0.38	-3.3
16	16:55:37-16:58:30	6.38	0.36	-1.9
17	17:18:22-17:21:01	19.52	0.36	-3.1
18	17:27:32-17:30:16	36.37	0.32	-3.3
19	17:39:40-17:42:27	16.19	0.32	-7.1
20	17:49:20-17:52:03	35.14	0.26	-3.1
21	17:59:47-18:02:25	41.67	0.35	-5.4
22	18:09:13-18:11:53	45.94	0.41	-18.3
23	18:21:31-18:24:32	63.4	0.32	11.0

Plume Dispersion Comparison

During each pass simulation, source strength, the 1 s averaged u^* (m s^{-1}), wind direction (°), and L (m) were input to the model. The average atmospheric parameters for each pass are listed in table 2.

Outputs were first compared with the LIDAR data by comparing the LIDAR-measured Gaussian plume dispersion parameters (σ_y and σ_z) with those calculated from the model run. Parameter σ_y (m) is the standard deviation of the cross-plume concentration distribution, and σ_z (m) is the standard deviation of the concentration distribution in the vertical direction. The dispersion parameters for the model were calculated directly from the output data. Corresponding σ_y and σ_z values were calculated from the LIDAR measurements of plume maximum concentrations (χ_{max}), horizontal (or vertical) plume edge concentrations (χ), and the distance between the points of maximum and the edge concentrations (∇i) after Hiscox et al. (2008):

$$\sigma_i = \frac{\left(\frac{\nabla i}{2}\right)^2}{-2\ln\eta} \tag{29}$$

where $\eta = \chi/\chi_{max}$, and $i = y, z$.

The comparisons of σ_y and σ_z were made at 10, 20, 40, 80, and 160 m in the downplume direction.

Overall, the ratio of simulated σ to measured σ ranged from 0.44 to 1.24, generally increasing with distance from the source, as shown in table 3. The table provides the measured and simulated mean plume σ_y and σ_z values at different distances. In the horizontal direction (σ_y), on average, the simulated value was smaller than the measured plume dispersion by 55% at 10 m and 39% at 20 m from the source, but was very close at farther distances. In the vertical direction (σ_z), the simulation underestimated the measurements (28%) near the source, was nearly equal at 80 m, and overestimated by 24% at 160 m away. The model prediction near the source was poorer than the prediction farther away. This was likely due to the motions of the tractor and the disking equipment modifying the nearby wind field and thus affecting the near-source plume dispersion.

Plume Shape Comparisons

Figure 6 shows a simulation of the model and the corresponding LIDAR measurements for pass 20. It plots (x, y) relative concentrations in horizontal slices through the plume at three heights and demonstrates the spatial patterns of the dust plume. Source strength was 350 μg s^{-1} and the simulation was run for 102 s from the tractor start time. The tractor speed was 1.47 m s^{-1}, mean u^* = 0.26 m s^{-1}, mean L = –3.1 m, and mean wind direction ψ = 35° during the whole 102 s simulation period. Figure 6 demonstrates similar patterns from the LIDAR measurements and from the model simulation in the location of the plume centerline and the maximum concentrations, which was further down plume at higher elevations. In addition, both show plume width increases with distance. These characteristics were expected, and the model captures them.

The LIDAR measurements show a bend in the plume downwind from the source where the dust plume was oriented in different directions at different distances, especially at the 3 m height. The model was able to capture these basic direction meanders due to the input of the short-time wind direction fluctuations. However, the model simulations were smoother with less spatial variability than the LIDAR observations. At the 15 m height, the LIDAR plume was broken up, most likely due to turbulent surface layer structures (eddies) on the scale of the plume. However, the model-simulated plume was a single connected plume. At 9 m height, the LIDAR measurements showed considerable spatial variability of concentration, especially showing a number of points of relatively large concentration, whereas the simulated plume demonstrated a more consistent dispersion inside the plume. Even at the 3 m height, the large-value points were more scattered in their distribution than the simulated plume.

We believe that much of the difference between the observations and the simulations is due to the fact that the

Table 3. Measured and simulated plume parameters and comparisons for the disking operations.

Downplume Distance (m)	σ_y Means (SD in parentheses)			σ_z Means (SD in parentheses)		
	Measured (m)	Simulated (m)	Ratio (meas./sim.)	Measured (m)	Simulated (m)	Ratio (meas./sim.)
10	7.9 (3.3)	4.0 (2.8)	0.44 (0.17)	6.1 (4.5)	3.8 (1.6)	0.72 (0.22)
20	9.3 (6.1)	5.3 (2.7)	0.61 (0.46)	6.8 (5.9)	4.7 (1.2)	1.01 (0.56)
40	8.5 (2.2)	9.3 (2.9)	1.2 (0.55)	9.3 (3.5)	6.3 (1.5)	0.85 (0.42)
80	14.9 (4.2)	13.9 (3.4)	1.06 (0.51)	9.8 (4.1)	9.1 (2.4)	1.02 (0.40)
160	22.3 (6.8)	17.6 (3.0)	0.91 (0.44)	11.0 (4.7)	11.8 (2.8)	1.24 (0.31)

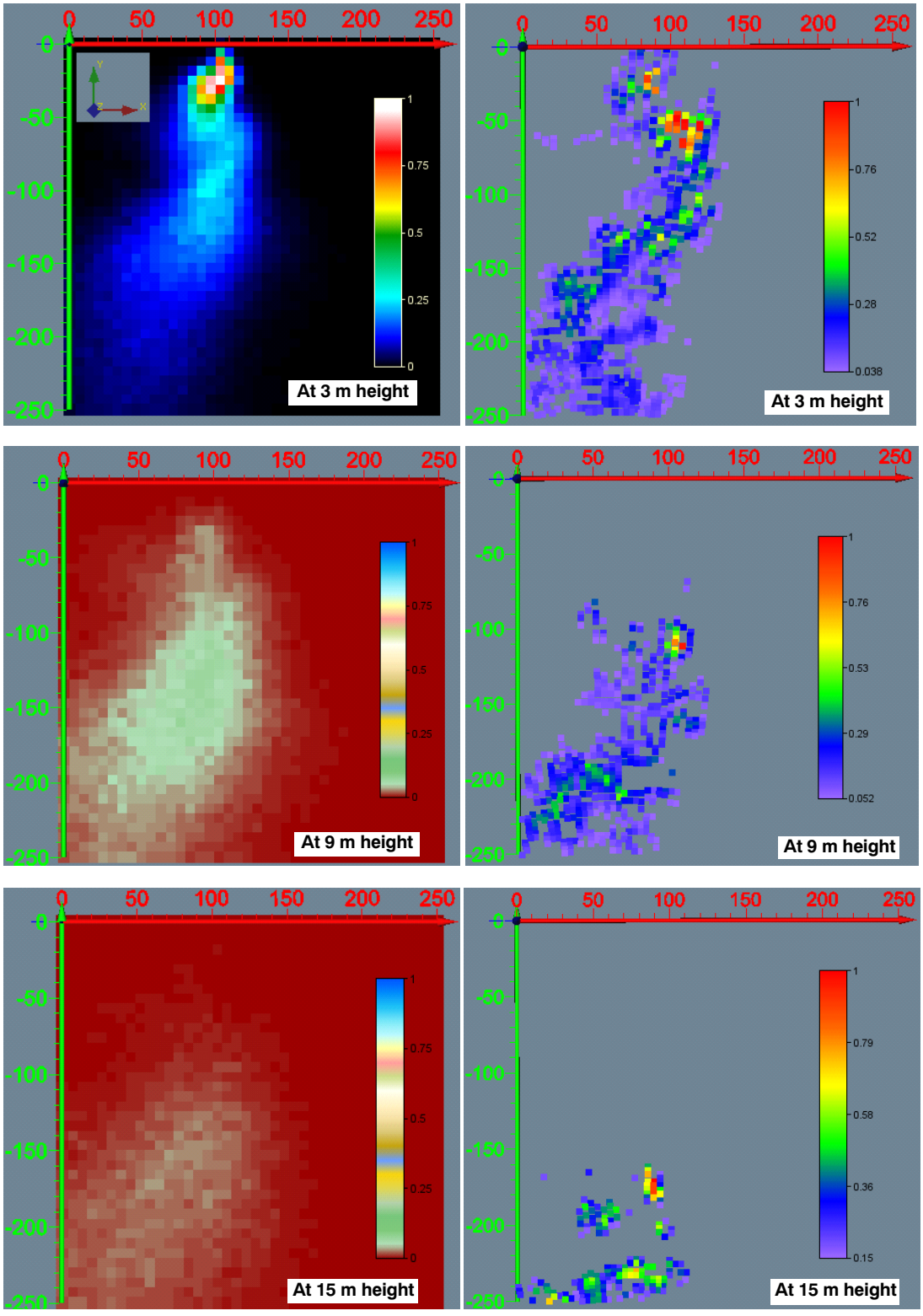

Figure 6. Comparison of model simulation (left) and observation (right) of instantaneous normalized dust concentration at different heights from a disking operation (pass 20) at 102 s after tractor started. LIDAR and simulated concentration data were divided by its maximum value at each height. Tractor traveled from right to left. Tractor start point is at (246, 0). Tractor speed = 1.47 m s^{-1}. The short-time (1 s) u^*, wind direction, and L were the model atmospheric inputs.

dynamic wind field and local convective eddies were not accurately represented over the whole simulation domain by measurements at one point in the field. Therefore, the model smoothes the dispersion spatially. To better simulate the dust dispersion, vertical wind speed, heat flux, and wind direction profiles at multiple horizontal points for dynamic wind variations are needed.

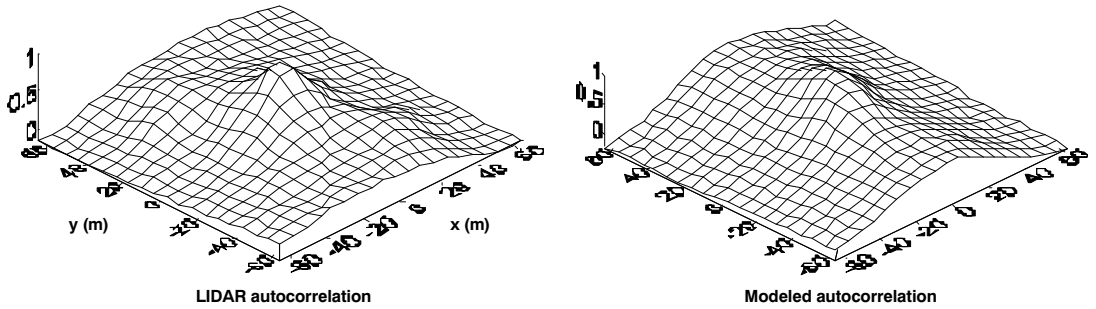

(a) 3 m height

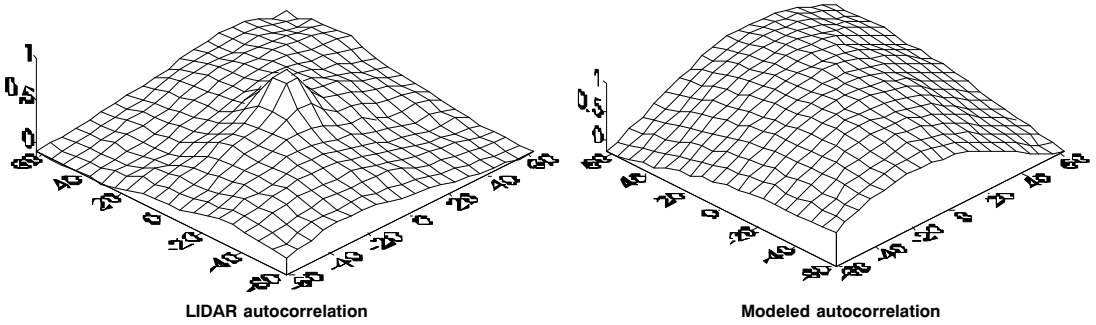

(b) 9 m height

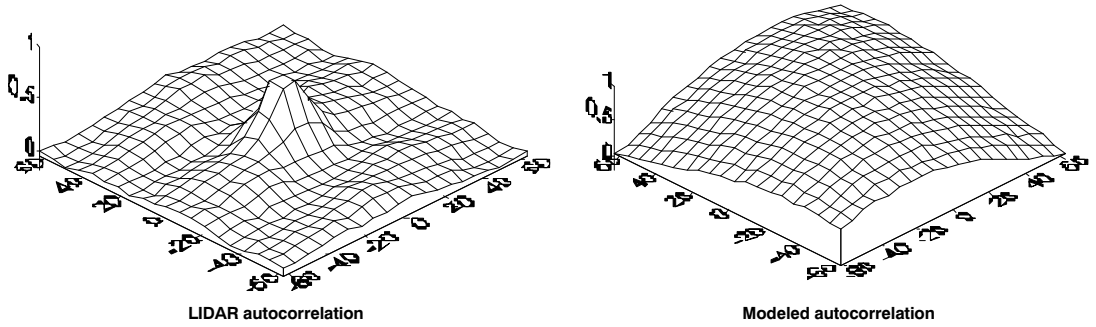

(c) 15 m height

Figure 7. Two-dimensional autocorrelation for the modeled domain in the *x*, *y* plane at (a) 3 m above ground, (b) 9 m above ground, and (c) 15 m above ground.

Statistical Comparison of Plume Concentrations and Locations

Two-dimensional spatial autocorrelation coefficients, shown in figure 7, were calculated (after Mayor et al., 2003) across the simulation domain for both the simulated concentrations (x, y) and the corresponding measured concentrations (x, y). The two dimensional autocorrelation, E, is:

$$E = \frac{N\sum a_i b_i - \sum a_i \sum b_i}{\left[N\sum a_i^2 - \left(\sum a_i\right)^2\right]^{1/2}\left[N\sum b_i^2 - \left(\sum b_i\right)^2\right]^{1/2}} \quad (30)$$

where a and b are the shifted x-y-oriented arrays, i is the index in either array (i.e., a_i and b_i are the ith elements in either array), and N is the number of points in either the a or b array (after Mayor et al., 2003).

Comparison of these coefficient plots allows the visualization of how closely matched are the intensity and locations of spatial clustering in the modeled and measured plumes. The following discussion describes these comparisons for one sample tractor pass (pass 20). The remaining passes from the field experiment are currently being analyzed, and their pass-to-pass characteristics and variability will be reported in a future article.

Figure 6a shows that the intensity and locations of spatial clustering are similar at 3 m above ground. But at 9 and 15 m above ground, the similarity breaks down. The steep variation of the autocorrelation coefficients with distance from the perfect correlation (1.00) at location (0,0) in the measured data versus the slow variation in the modeled data demonstrates that the model smoothes the dispersion process by moving individual particles rather than moving high-concentration clumps of particles as measured by the LIDAR. The clumping of aerosols is caused by eddies and gusts breaking up the plume, which the model does not capture.

In order to quantify the pattern correlation between the simulated and measured concentrations, two-dimensional spatial cross-correlations were calculated after Mayor et al. (2003) and are shown in figure 8. Equation 30 was used where the a array was the LIDAR data and the b array was the simulated data.

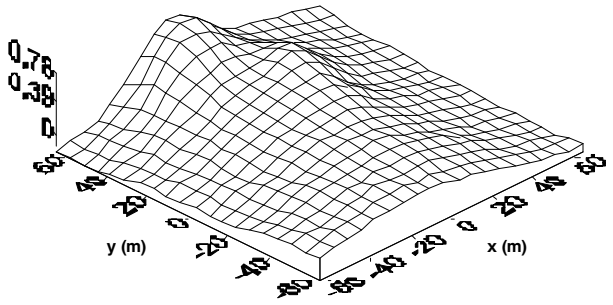

Maximum cross-correlation coefficient = 0.78

(a) 3 m height

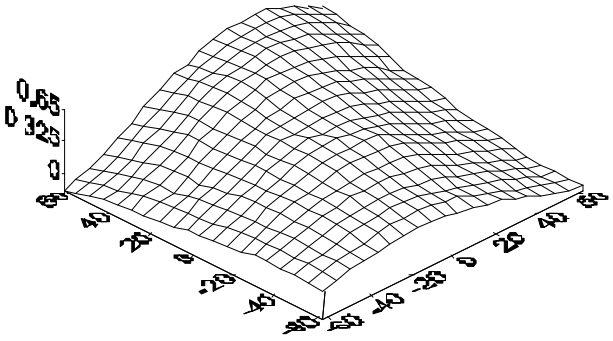

Maximum cross-correlation coefficient = 0.65

(b) 9 m height

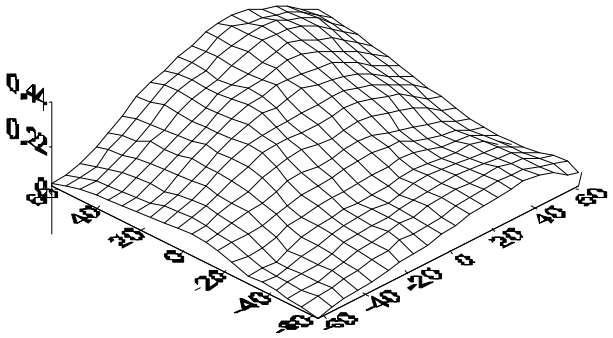

Maximum cross-correlation coefficient = 0.44

(c) 15 m height

Figure 8. Two-dimensional cross-correlation between the LIDAR measured and the modeled dust concentrations at (a) 3 m above the ground, (b) 9 m above the ground, and (c) 15 m above the ground.

Figure 8a shows the 3 m cross-correlation coefficients, which have a peak coefficient of 0.78. This high correlation implies a close spatial pattern similarity between the measured and modeled plumes. The peak location (at –6 m, 58 m) indicates that the modeled plume was offset from the measured plume by 6 m in the *x* direction and 58 m in the *y* direction.

Figure 8b and 7c show lower peak correlations, 0.65 at 9 m height and 0.44 at 15 m height, farther from the origin (0,0), indicating a decreasing pattern correlation with increasing height above the ground. The maximum coefficient is at (x = 20 m, y = 44 m) at the 9 m and 15 m heights, indicating that the offset distances are larger than at the 3 m height.

As discussed earlier, we believe that the lower similarity at higher heights between measured and modeled concentration patterns is due to the fact that the dynamic wind field was not accurately represented at higher heights by a sonic wind measurement at a single height (1.5 m).

Finally, neither the point measurements nor the LIDAR measurements included dust suspended closer to the ground than 1.5 m (Holmén et al., 2008). Therefore, only the particles reaching that height were modeled. It is likely that larger particles were emitted into the air by the disk but fell to the ground quickly, or remained suspended near the ground, never reaching the sensor height. Based on Stoke's law, when the dust particle size is 20 μm, the settling speed will be 0.025 m s^{-1} , 0.057 m s^{-1} for 30 μm, 0.1 m s^{-1} for 40 μm, and 0.4 m s^{-1} for 80 μm. Therefore, particles up to 40 μm, which would take longer than 15 s to fall (1.5 m / 0.1 m s^{-1}), could have drifted off the field near the surface and not been included in this modeling effort.

CONCLUSIONS

The dynamic Lagrangian PM_{10} transport model presented here is capable of simulating near-field dust dispersion from agriculture field operations. Its major advantages over other existing near-field models are that it can simulate moving sources and plume meander. The simulated plume spread parameters (σ_y, σ_z) at downplume distances up to 160 m were within ±73% of those measured with a remote aerosol LIDAR. Cross-correlations between a modeled plume and LIDAR measurements of the actual plume were as high as 0.78 near the ground and decreased to 0.65 at 9 m above ground, indicating close pattern similarity between the modeled and measured plumes at lower heights above ground. The model can be used to predict and assess the dust emissions and in-field and near-field human exposures from field agriculture operations. To better simulate the dust dispersion, vertical wind speed and wind direction profiles at multiple horizontal points for dynamic wind variations should be considered.

ACKNOWLEDGEMENTS

This work was supported with funds from the USDA NRI CSREES program under Contract No. 2004-35112-14230, the University of Connecticut Storrs Agricultural experiment station, and the New Mexico State University Agricultural Experiment Station. The authors are grateful to the staff at the Agricultural Experiment Station at New Mexico State University for their generous cooperation during the field experiments.

REFERENCES

Aylor, D. E., and F. J. Ferrendino. 1989. Dispersion of spores released from an elevated line source within a wheat canopy. *Boundary-Layer Meteorol.* 46(3): 251-273.

Aylor, D. E., and T. K. Flesch. 2001. Estimating spore release rates using a Lagrangian stochastic simulation model. *J. Appl. Meteorol.* 40(7): 1196-1208.

Campbell, G. S., and J. M. Norman. 1998. *An Introduction to Environmental Biophysics*. 2nd ed. New York, N.Y.: Springer-Verlag.

Chow, J. C., J. G. Watson, M. C. Green, D. H. Lowenthal, D. W. DuBois, S. D. Kohl, R. T. Egami, J. A. Gillies, C. F. Rogers, C. A. Frazier, and W. Cates. 1999. Middle- and neighborhood-scale variations of PM_{10} source contributions in Las Vegas, Nevada. *J. Air and Waste Mgmt. Assoc.* 49(6): 641-654.

Coirier, W. J., and S. Kim. 2006a. CFD modeling for urban area contaminant transport and dispersion: Model description and data requirements. In *Preprints 6th Symp. on the Urban Environment*, JP2.11. Boston, Mass.: American Meteorological Society.

Coirier, W. J., and S. Kim. 2006b: Summary of CFD-Urban results in support of the Madison Square Garden and Urban Dispersion Program field texts. In *Preprints 6th Symp. on the Urban Environment*, JP5.5. Boston, Mass.: American Meteorological Society.

Csanady, G. T. 1963. Turbulent diffusion of heavy particles in the atmosphere. *J. Atmos. Sci.* 20(3): 201-208.

EPA. 1995. User's guide for the industrial source complex (ISC3) dispersion models. Research Triangle Park, N.C.: U.S. EPA, Office of Air Quality Planning and Standards Emissions, Monitoring, and Analysis Division.

Etyemezian, V., J. Gillies, H. Kuhns, D. Nikolic, J. Watson, J. Veranth, R. Labban, G. Seshadri, and D. Gillette. 2003. Field testing and evaluation of dust deposition and removal mechanisms. Final report. Prepared for the Western States Air Resources (WESTAR) Council, Lake Oswego, Ore.

Etyemezian, V., S. Ahonen, D. Nikolic, J. Gillies, H. Kuhns, D. Gillette, and J. Veranth. 2004. Deposition and removal of fugitive dust in the arid southwestern United States: Measurements and model results. *J. Air and Waste Mgmt. Assoc.* 54(9): 1099-1111.

Flaherty, J. E., K. J. Allwine, M. J. Brown, W. J. Coirier, S. C. Ericson, O. R. Hansen, A. H. Huber, S. Kim, M. J. Leach, J. D. Mirocha, R. K. Newsom, G. Patnaik, and I. Senocak. 2007. Evaluation study of building-resolved urban dispersion models. In *Preprints 7th Symp. on the Urban Environment*, 10.2. Boston, Mass.: American Meteorological Society.

Flesch, T. K., and J. D. Wilson. 1992. A two-dimensional trajectory-simulation model for non-Gaussian, inhomogeneous turbulence within plant canopies. *Boundary-Layer Meteorol.* 61(4): 349-374.

Hamel, D. M. Chwastek, B. Farouk, K. Dandekar, and M. Kam. 2006. A computational fluid dynamics approach for optimization of a sensor network. In *Proc. IEEE Intl. Workshop on Measurement Systems for Homeland Security, Contraband Detection, and Personal Safety.* Piscataway, N.J.: IEEE.

Hanna, S. R., G. A. Briggs, and R. P. Hosker. 1982. *Handbook on Atmospheric Diffusion*. DOE/TIC-11223 (DE82002045). Washington, D.C.: U.S. Department of Energy, Technical Information Center.

Haupt, S. E., G. Young, A. Beyer, and K. Long. 2007. Assimilating sensor concentration data into a dispersion model in a meandering flow field. In *Proc. 11th GMU Conf. on Atmospheric Transport and Diffusion*. Fairfax, Va.: George Mason University.

Hiscox, A. L., D. R. Miller, and C. Nappo. 2006. A note on the use of lidar images of smoke plumes to measured dispersion parameters in the stable boundary layer. *J. Atmos. and Oceanic Tech.* 23(8): 1150-1154.

Hiscox, A. L., D. R. Miller, B. A. Holmén, W. Yang, and J. Wang. 2008. Near-field dust exposure from cotton field tilling and harvesting. *J. Environ. Quality* 37(2): 551-556.

Holmén, B. A., D. R. Miller, A. L. Hiscox, W. Yang, T. W. Sammis, and R. Bottoms. 2008. Near-source particulate emissions and plume dynamics from agricultural field operations. *J. Atmos. Chem.* 59(2): 117-134.

Mayor, S. D., G. J. Tripoli, and E. W. Eloranta. 2003. Evaluating large-eddy simulations using volume imaging LIDAR data. *Monthly Weather Review* 131(7): 1428-1452.

Panofsky, H. A., and J. A. Dutton. 1984. *Atmospheric Turbulence: Models and Methods for Engineering Applications*. New York, N.Y.: Wiley.

Panofsky, H. A., H. Tennekes, D. H. Lenschow, and J. C. Wyngaar. 1977. The characteristics of turbulent velocity components in the surface layer under convective conditions. *Boundary-Layer Meteorol.* 11(3): 355-361.

Sawford, B. L., and F. M. Guest. 1991. Lagrangian statistical simulation of the turbulent motion of heavy particles. *Boundary-Layer Meteorol.* 54(1-2): 147-166.

Stull, R. B. 2001. *An Introduction to Boundary Layer Meteorology.* Dordrecht, The Netherlands: Kluwer Academic.

Thomson, D. J. 1987. Criteria for the selection of stochastic models of particle trajectories in turbulent flows. *J. Fluid Mech.* 180: 529-556.

USDA-NRCS. 2005. Soil Survey Geographic (SSURGO) database for Dona Ana County area, New Mexico. Fort Worth, Texas: USDA-NRCS.

Van den Hurk, B. J. J. M., and D. D. Baldocchi. 1990. Random-walk models for simulating water vapor exchange within and above a soybean canopy. NOAA Technical Memorandum ERL ARL-185. Silver Spring, Md.: NOAA Air Resources Laboratory.

Veranth, J. M., E. Pardyjak, G. Seshadri, E. Kaser, and F. Yin. 2004. Measurement of fugitive dust suspension and redeposition under Dona Ana County, New Mexico, conditions. SCERP Report of Project No. A-02-07. San Diego, Cal.: Southwest Consortium for Environmental Research and Policy.

Wagner, L. E., and L. J. Hagen. 1998. Application of WEPS-generated soil loss components to assess off-site impacts. ASAE Paper No. 982057. St. Joseph, Mich.: ASAE.

Wang, Y., D. R. Miller, D. E. Anderson, and M. L. McManus. 1995. A Lagrangian stochastic model for aerial spray transport above an oak forest. *Agric. and Forest Meteorol.* 76(3-4): 277-291.

Wilson, J. D., and W. K. N. Shum 1992. A re-examination of the integrated horizontal flux method for estimating volatilization from circular plots. *Agric. and Forest Meteorol.* 57(4): 281-295.

Appendix

Symbols Used in the Random-Walk Model.

a_i	= ith element of the shifted x-oriented array
b_i	= ith element of the shifted y-oriented array
$c_{2000}(X, Y, Z, t)$	= 2000 nm particle concentration at point (X, Y, Z) and time t (μg m^{-3})
$c_{4041.6}(X, Y, Z, t)$	= 4041.6 nm particle concentration at point (X, Y, Z) and time t (μg m^{-3})
$c_{total}(X, Y, Z, t)$	= simulated total concentration (PM_{10}) at point (X, Y, Z) and time t (μg m^{-3})
$c_{PM\ 10}(X, Y, Z, t)$	= actual (scaled by input source strength) PM_{10} concentration at point (X, Y, Z) and time t (μg m^{-3})
c_u	= parameter for turbulence velocity calculation (dimensionless)
c_w	= parameter for turbulence velocity calculation (dimensionless)
dt	= time step of one flight (s)
dx	= displacement on x axis during dt (m)
dy	= displacement on y axis during dt (m)
dz	= displacement on z axis during dt (m)
E	= two-dimensional autocorrelation (dimensionless)

H = particle release height (m)
k = Karman constant (0.4)
L = Monin-Obukhov length (m)
l = length scale (m)
P_G = fraction of a grain deposited which reaches ground (dimensionless)
P_{N2000} = 2000 nm particle number
Q = source strength input (350 μg s^{-1})
Q_{si} = source strength in the simulation (μg s^{-1})
q_u = parameter for along-wind turbulence calculation (dimensionless)
q_v = parameter for cross-wind turbulence calculation (dimensionless)
q_w = parameter for vertical turbulence calculation (dimensionless)
R_n = random number chosen from a uniform distribution between 0 and 1 (dimensionless)
r_u, r_v, r_w = random Gaussian variables (dimensionless)
t = time (s)
t_{max} = maximum time for a particle to disperse to the downwind edge of a implement (s)
T_{re} = puff release time (s)
u^* = friction velocity (m s^{-1})
$\bar{u}(z)$ = mean horizontal wind velocity at height of z (m s^{-1})
u = along-wind turbulent velocity (m s^{-1})
v = cross-wind turbulent velocity (m s^{-1})
V_d = implement-induced upwardly displaced air velocity (m s^{-1})
V_{2000} = volume of each 2000 nm particle (m^3)
v_s = settling velocity of a particle (m s^{-1})
V_{tr} = tractor speed (m s^{-1})
w = vertical turbulent velocity (m s^{-1})
X = coordinate in tractor traveling direction (m)
x = coordinate in wind direction (m)
Y = coordinate in the direction perpendicular to the tractor traveling direction (m)
y = coordinate in the cross-wind direction (m)
Z = height above ground (m)
z = height above ground (m)
z_i = mixing layer height (m)
z_{t-1} = position of the particle at the previous time step (m)
z_0 = roughness length (m)
α = parameter for turbulent velocity calculation (dimensionless)
β = parameter for turbulent velocity calculation (dimensionless)
γ = parameter for turbulent velocity calculation (dimensionless)
η = χ/χ_{max} (dimensionless)
χ_{max} = LIDAR measured maximum concentration for plume parameter calculation (dimensionless)
χ = LIDAR measured edge concentration for plume parameter calculation (dimensionless)
θ = angle between the x and X axes (degrees)
ρ = particle density (μg nm^{-3})
σ_i = plume parameter, $I = y, z$ (m)
σ_u = standard deviation of wind velocity in mean wind direction (m s^{-1})
σ_v = standard deviation of wind velocity in cross-wind direction (m s^{-1})
σ_w = standard deviation of vertical wind velocity (m s^{-1})
τ_L = Lagrangian time scale (s)
φ = stability correction term (dimensionless)
χ = random Gaussian variable (dimensionless)
ψ = wind direction (degrees)
∇i = distance between the points of maximum concentration and the edge concentration, $I = y, z$ (m)
∇V = detection cube volume (m^3)